Urban Climate 28 (2019) 100458

Contents lists available at ScienceDirect

Urban Climate

journal homepage: www.elsevier.com/locate/uclim

Spatial differentiation of urban wind and thermal environment in different grid sizes

Jun Yang[a,b,*], Yichen Wang[a], Xiangming Xiao[c,d,**], Cui Jin[a], Jianhong (Cecilia) Xia[e], Xueming Li[a]

[a] *Human Settlements Research Center, Liaoning Normal University, Dalian 116029, China*
[b] *Jangho Architecture College, Northeastern University, Shenyang 110169, China*
[c] *Department of Microbiology and Plant Biology, Center for Spatial Analysis, University of Oklahoma, Norman, OK 73019, USA*
[d] *Ministry of Education Key Laboratory of Biodiversity Science and Ecological Engineering, Institute of Biodiversity Science, Fudan University, Shanghai 200433, China*
[e] *School of Earth and Planetary Sciences, Curtin University, Perth 65630, Australia*

ARTICLE INFO

Keywords:
Frontal area index
Urban thermal environment
Grid size
Maximum mutual information
Dalian city

ABSTRACT

Due to rapid urbanization, China's urban morphology has undergone tremendous changes, resulting in an increased urban heat island (UHI) effect and negative impact of thermal environment, especially in summer. Studying the scale effect between urban wind and thermal environment can provide the best scale for the wind environment planning on mitigating UHI effect. Taking Dalian as an example, using multi-source data, a nonlinear correlation analysis was used to analyze the correlation between the frontal area index (FAI) and land 77uuyyhsurface temperature (LST) under different grids. The results show that first, FAI is sensitive to grid-size changes. When the grid size increases from 25 × 25 m to 150 × 150 m with a step size of 25 m, in July, the numbers of grids with FAI > 1 are 19,992, 1538, 153, 20, 4, and 0 (0%) accounting for 2.106%, 0.645%, 0.081%, 0.019%, 0.006%, and 0% of the total, respectively. In September, the numbers of grids with FAI > 1 are 17,633, 1643, 164, 22, 8, and 0, accounting for 1.849%, 0.689%, 0.155%, 0.037%, 0.021%, and 0% of the total, respectively. When the grid size is greater than or equal to 150 × 150 m, there is no grid with FAI > 1. Second, the most effective grid size to study the relationship between FAI and LST is 25 m. When the grid size increases from 25 m to 300 m with a step size of 25 m, the correlation between FAI and LST shows a significant decrease. When the grid size is 25 m, the correlation is the strongest.

1. Introduction

Urban thermal environment refers to the physical environment related to heat affecting the human body's perception of cold and warmth, health level, and human survival and development. The urban heat island (UHI) effect refers to the phenomenon where the temperature in urban areas is significantly higher than that in the surrounding rural areas (Rizwan et al., 2008). UHI is a concentrated expression of urban thermal environment. Rapid urbanization leads to changes in building morphology, surface properties, and increasing crowds in cities(Yang et al., 2018b, 2018a; Liu et al., 2018). These factors have changed the energy balance dramatically,

* Correspondence to: J. Yang, No. 850 Huanghe Road, ShaHekou District, Dalian City, Liaoning Province 116029, China.
** Correspondence to: X. Xiao, Department of Microbiology and Plant Biology, Center for Spatial Analysis, University of Oklahoma, Norman, OK 73019, USA.
E-mail addresses: yangjun@lnnu.edu.cn (J. Yang), xiangming.xiao@ou.edu (X. Xiao), cuijin@lnnu.edu.cn (C. Jin), c.xia@curtin.edu.au (J.C. Xia).

https://doi.org/10.1016/j.uclim.2019.100458
Received 10 September 2018; Received in revised form 6 January 2019; Accepted 20 March 2019

and they make UHI more intense. UHI can strengthen heat waves, which in turn enhance the negative impact of UHI, leading to a deterioration of the quality of urban thermal environment (Clarke and Bach, 1971). This results in urban residents facing a higher health risk (Jandaghian and Akbari, 2018; Tan et al., 2010), a higher energy cost (Konopacki and Akbari, 2000) and affacting human acitvities (Chen et al., 2017a). UHI can be divided into surface heat island (SUHI), canopy heat island (CUHI), and boundary heat island (BUHI). SUHI has been proved to be an important factor for thermal environment (Li et al., 2018b). It can be measured by land surface temperature (LST), which has been widely applied in UHI studies (Qiao et al., 2013; Voogt and Oke, 2003; Zhou et al., 2014).

Rapid urbanization has changed urban landscape patterns by increasing building surface area and complex morphology. The complex structure and spatial pattern directly cause obstacles and disturbances to the wind (Allegrini and Carmeliet, 2017; Qiao et al., 2017; Yang et al., 2019). Due to the blocking effect of wind, heat and pollutants accumulate in densely populated areas, thereby affecting urban thermal environment (Estoque et al., 2017) and urban air pollution (Li et al., 2018a). In addition, buildings can affect radiation transfer processes, indirectly influencing UHI (Li et al., 2019). The urban wind environment, which refers to the wind field, is dependent on the distribution of non-mechanical ventilation and generated by gradients in urban wind and thermal pressure. Ventilation allows heat to diffuse and reduce pollutant concentration (He et al., 2019). Therefore, it is important to study wind environment and urban space thermal environment to reduce the negative impact of the UHI effect. Previous research on urban wind environment mainly involves two layers: urban boundary layer and urban canopy layer. Some studies have further divided the urban canopy layer. Ng et al. (2011) sampled and calculated the heights of buildings in Hong Kong and further divided the urban canopy layer (0–60 m) into podium layer (0–15 m) and building layer (15–60 m). The methods used in urban wind environment studies include wind tunnel model (Brunet et al., 1994; Gromke, 2018), computational fluid dynamics (CFD) simulation (Dhunny et al., 2018; Wang et al., 2018), and urban morphological parameters. Compared with others, urban morphological parameters, which are widely used, can accurately describe the aerodynamic characteristics of cities and explain most urban climate phenomena and processes with a lower cost. Frontal area index (FAI) is an important indicator of the blocking effect of buildings and is usually used to study urban wind environment. It refers to the ratio of the projected area along the fixed wind direction to the area of the calculation unit (Lettau, 1969). It has a similarity with the roughness parameter as both can describe urban morphology and the blocking effect of wind in cities (Macdonald et al., 1998). However, the influence of wind direction considered in FAI calculation makes FAI more objective in evaluating urban wind environment. Bottema and Mestayer first calculated and made an FAI map (Bottema and Mestayer, 1998). FAI was used to construct a model for predicting wind speed ratio (Ikegaya et al., 2017) and evaluating urban wind environment (Chen et al., 2017b,c; Yuan et al., 2014). By affecting wind environment, FAI has an impact on both urban thermal environment and atmospheric pollution (Cariolet et al., 2018). In order to improve wind environment and alleviate various negative environmental problems in an urban area, a method of applying an FAI map and least cost path (LCP) analysis is widely used to evaluate ventilation corridors inside a planned dense city (Chen et al., 2017b; Hsieh and Huang, 2016; Peng et al., 2017a; Wong et al., 2010). Furthermore, the relationship between urban morphology and UHI could be different in different periods (Zhang et al., 2016). However, cities are facing the impact of a higher temperature during summer. The existence of the UHI effect exacerbates the much higher temperature in urban areas, creating a high health risk. Therefore, the study of UHI in summer by urban form plays an important role in improving urban ventilation and easing high temperatures.

The landscape pattern is scale-dependent (Wu, 2004). At a certain scale, the correlation among elements may be stronger. Generally, the ideal scales are different in different regions (Lan and Zhan, 2017). Scale dependence is widely discussed in studies on LST and FAI. Scale dependence studies on LST include the optimal scale for correlation between landscape structure and LST (Song et al., 2014; Wang et al., 2016), and the measurement of vegetation–temperature correlation (Fan et al., 2015). The scale dependence of FAI stems from calculation units. There are two types of calculation units: polygonal blocks occupied by buildings (Burian et al., 2002; Gál and Unger, 2009), and the regular-shaped grid of certain areas dividing the study area. Existing research mainly uses regular-shaped grids as calculation units. The mentioned grid size or scale of FAI is the size of this defined regular-shaped grid. Previous studies have various perspectives on the choice of grid size (Table 1).

Studies considering the scale effects of the connection between urban wind and thermal environment are sparse. Taking Dalian as an example, this study analyzes the correlation between FAI and LST under different grid sizes based on multi-source data, such as building and remote sensing data. It also examines the scale dependence of FAI calculation, determines the most effective grid size for FAI calculation in studies on urban issues, clarifies the scale effect between wind environment and urban thermal environment, and

Table 1
Grid sizes of frontal area index in previous studies.

Year	Researcher	Study Area	Grid Size
1998	Bottema	Strasbourg, France	150 × 150 m
2010	M.S.Wong	Kowloon Peninsula, Hong Kong, China	100 × 100 m
2011	Edward Ng	Kowloon Peninsula, Hong Kong, China	200 × 200 m
2013	M.S.Wong	Kowloon Peninsula, Hong Kong, China	100 × 100 m
2013	J.Y.Liu	Yuexiu District, Guangzhou City, Guangdong Province, China	250 × 250 m
2016	S.L.Chen	Renhuai, Zunyi City, Guizhou Province, China	100 × 100 m
2016	F. Peng	Kowloon Peninsula, Hong Kong, China	30 × 30 m
2017	F. Peng	Kowloon Peninsula, Hong Kong, China	10 × 10 m
2017	Y.Xu	Kowloon Peninsula, Hong Kong, China	10 × 10 m
2017	Y.C.Chen	Tainan, Taiwan, China	50 × 50 m

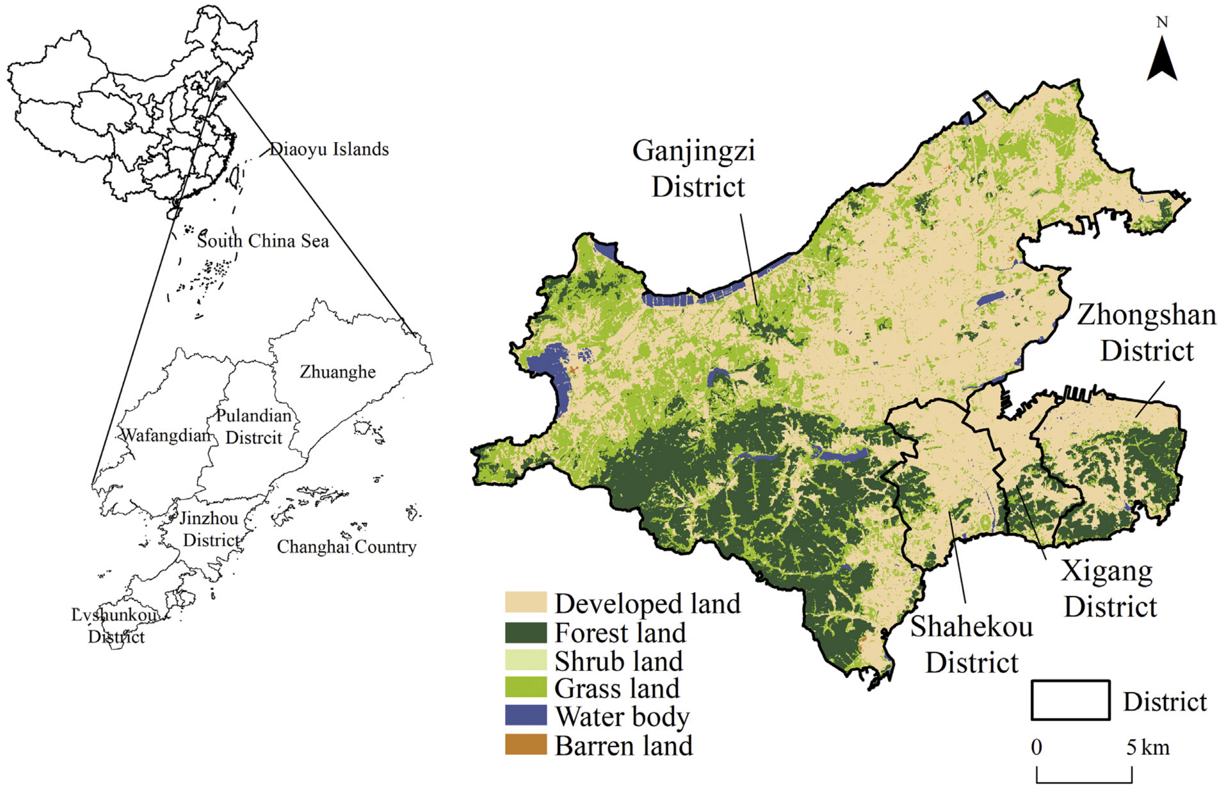

Fig. 1. Location of the study area.

provides the best scale reference for wind environment planning strategies on mitigating the UHI effect.

2. Data and methods

2.1. Study area

Dalian is located between 121.275°–121.750° E and 38.813°–39.087° N, and experiences a monsoon-influenced humid continental climate. According to the distribution of buildings, we choose the downtown area of Dalian as the study area, including four

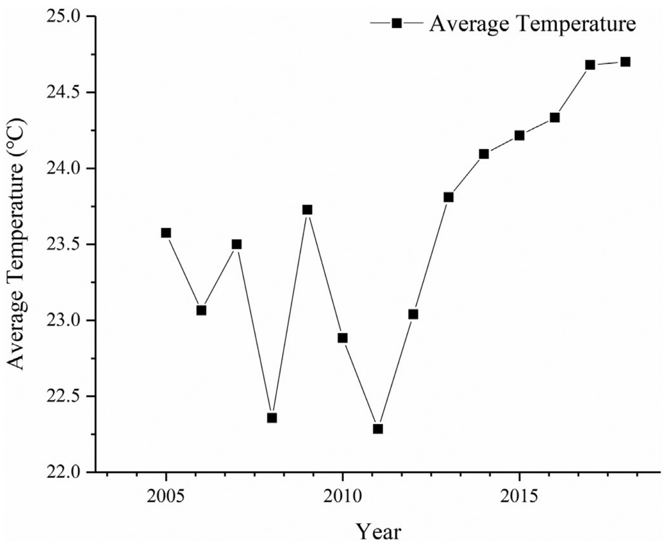

Fig. 2. Average temperature in summer (June to August) from 2005 to 2018.

Table 2
Data sources and descriptions.

Type of data	Descriptions	Source
Remote sensing data	Landsat8 OLI (Spatial resolution 30 m) Landsat8 TIRS (Spatial resolution 100 m) 2016-7-2 02:34:00 GMT+ 2017-9-23 02:34:00 GMT+	http://gscloud.cn
Meteorological data	Observation data of meteorological stations (air temperature and wind direction data from 2005 to 2017 in July and September)	http://rp5.ru
Building data	Building outline, floor and type	Baidumap
Administrative division data	Administrative division data of the country, province, city, county (district), township (town, street)	

administrative districts—Zhongshan, Xigang, Shahekou, and Ganjingzi—(Fig. 1), covering an area of 620 km^2. As shown in Fig. 2, the average temperature in Dalian in summer (June–August) from 2005 to 2018 has been increasing year by year. The average temperature in summer in 2018 is the highest, at 24.7 °C.

2.2. Data sources

The research data include Landsat-8 OLI/TIRS, building data, and meteorological record, as shown in Table 2. According to the acquisition time of the building data and the cloud amount of the remote sensing image, two Landsat 8 images were selected and band 10 was used to invert the land surface temperature. The building data contains building outlines and floors and types, as shown in Fig. 3. FAI calculation requires the height of each building; therefore, a method for calculating the building height using floor information and average floor height was used in this study. Different types of buildings have different average floor height; according to the Dalian City Planning and Architectural Design Regulations (Bureau of Urban Planning Dalian China, 2004), the residential building floor average height is set at 3 m, and the public building floor average height is set at 5 m, as shown in Table 3.

2.3. Research methods

2.3.1. Frontal area index

The equation for calculating FAI (Wong et al., 2010) is as follows:

$$\lambda_{f(\theta)} = A(\theta)/A_{plane} \tag{1}$$

θ represents the wind direction angle, A(θ) represents the projected area of the building in a specific wind direction, and A_{plane} represents the area of the calculation unit. The larger is the value of $\lambda_{f(\theta)}$, the greater is the hindrance to the wind. The value of $\lambda_{f(\theta)}$ varies with different wind directions. In order to objectively reflect the obstructive effect of buildings on the wind, we adopted wind directions for the months when the remote sensing images were taken, that is, from 2005 to 2017. We calculated the wind frequency and added weights to FAI. The equation is as follows:

$$\lambda_f = \sum_{n=1}^{16} \lambda_{f(\theta)} \cdot P_\theta \tag{2}$$

P_θ represents the wind frequency in the θ direction. This study adopted the 16 compass orientation method. The FAI calculation methods can be divided into grid and vector algorithms according to the data used. Grimmond and Oke (1999) and Burian et al. (2002) proposed a well-developed FAI algorithm using vector data. Similarly, Wong (Wong et al., 2010) considered the occlusion of buildings. Chen et al. (2017c) examined the local terrains affecting wind environment. Ratti et al. (2002) first proposed an FAI algorithm using raster data. Peng et al. (2017b) and Xu et al. (2017) extracted the FAI algorithm based on Lidar and SAR data, respectively. Using building vector data and recorded data from the weather station, we calculated FAI and weighted it with wind frequency.

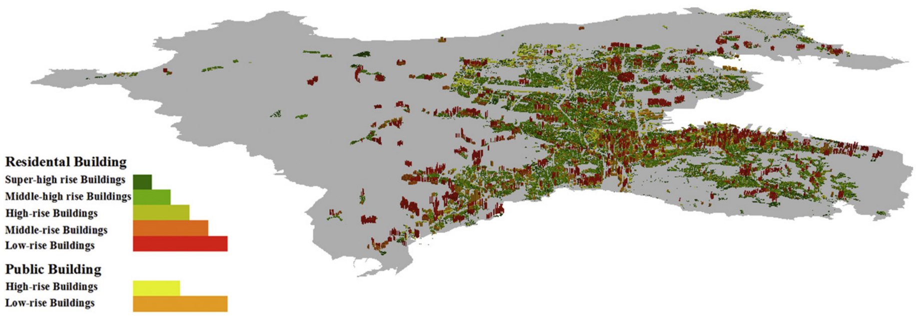

Fig. 3. 3D display of building data.

Table 3
Standard for floors classification of buildings.

Type	Floors classification	Average floor height(m)
Residential buildings	0–3 Low-rise buildings 4–6 Middle-rise buildings 7–9 High-rise buildings 10–12 Middle-high rise buildings > 12 Super-high rise buildings	3 m
Public buildings	0–4 Low-rise buildings > 4 High-rise buildings	5 m

2.3.2. LST inversion

This study used a single-window algorithm proposed by Qin et al. (2001) and Wang et al. (2015), which has been proven to provide good results for the inversion of surface temperature (Hu et al., 2015). The specific equations are as follows:

$$T_S = \{a(1 - C - D) + [b(1 - C - D) + C + D]T - DT_a\}/C \tag{3}$$

$$\mathrm{C} = \tau\varepsilon \tag{4}$$

$$\mathrm{D} = (1 - \tau)[(1 - \varepsilon)\tau] \tag{5}$$

T_s represents LST (K), and a and b represent coefficients obtained by fitting the relationship between heat radiation intensity and brightness temperature. When brightness temperature is 10 °C to 40 °C, a = −67.355351, b = 0.458606; ε is land surface emissivity; τ is atmospheric transmissivity in thermal infrared band; T is at-sensor brightness temperature; and Ta is the mean atmospheric temperature (K), which can be calculated by the parameter estimation method proposed as follows:

1) Brightness temperature: TIRS band 10 data are thermal infrared bands with corresponding pixel brightness temperatures as follows:

$$\mathrm{T} = \mathrm{K2}/ln(K1/L\lambda + 1) \tag{6}$$

where Lλ represents radiation intensity received by the sensor; K1 and K2 represent prelaunch preset constants found in the Landsat 8 header files; and K1 = 774.89, K2 = 1321.08.

2) Mean atmospheric temperature: Mean atmospheric temperature (Ta) generally depends on the profile of atmospheric air temperature distribution and atmospheric conditions. Qin et al. (2001) demonstrated that mean atmospheric temperature (Ta) has a linear relationship with near-surface temperature (T0). We obtain T0 from the same period of meteorological data. Given that the study area is located in the mid-latitudes and that the images were acquired during July and September, mean mid-latitude summer atmospheric conditions were therefore used:

$$\mathrm{Ta} = 16.0110 + 0.9262\mathrm{T0} \tag{7}$$

2.3.3. Correlation analysis and trend test

Correlation analysis was used to test the grid size corresponding to the strongest correlation between LST and FAI. Because FAI has a complex relationship with wind speed and LST, it is more appropriate to use a nonlinear correlation coefficient than a linear one (e.g., the Pearson correlation coefficient). This study used maximal information coefficient (MIC) (Reshef et al., 2011) to characterize the correlation. MIC can be used to find not only linear relationships but also nonlinear relationships between variables, and not only function relationships but also non-function relationships (e.g., the superposition of function relationships). The equation is as follows.

$$\mathrm{MIC} = max_{|x||y| < B}\, I[x;y]/log_2(min(|x|, |y|)) \tag{8}$$

The Mann–Kendall trend test (Kendall, 1975) was used to analyze the changing trend of the correlation with the change of grid size. The process is as follows. Define the test statistic S:

$$\mathrm{S} = \sum_{i=2}^{n} \sum_{j=1}^{i-1} sign(X_i - X_j) \tag{9}$$

In Eq. (9), the values of sign ($X_i - X_j$) are as follows:

$$\mathrm{sign}(X_i - X_j) = \begin{cases} -1\ (X_i - X_j) < 0 \\ 0\ (X_i - X_j) = 0 \\ 1\ (X_i - X_j) > 0 \end{cases} \tag{10}$$

Given $n \geq 10$, when S is greater than, equal to, or less than zero, the M-K statistic is as follows, respectively.

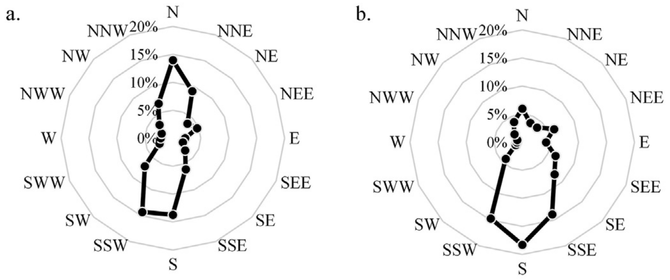

Fig. 4. Wind direction frequencies (a. July, b. September).

$$Z = \begin{cases} (S - 1)/\sqrt{\mathrm{Var}(S)} & S > 0 \\ 0 & S = 0 \\ (S + 1)/\sqrt{\mathrm{Var}(S)} & S < 0 \end{cases} \tag{11}$$

A positive value for Z indicates an increasing trend and a negative value indicates a decreasing trend. When the absolute value of Z is greater than or equal to 1.65, 1.96, and 2.58, it indicates that the significance level is 90%, 95%, and 99%, respectively.

3. Analysis of results

3.1. Frontal area index distribution

This study calculated the observations of wind directions at the meteorological site in the study area in July and September from 2005 to 2017, and the wind frequency in each direction using the 16 compass positions, as shown in Fig. 4. The main prevailing wind directions in the study area were south (18.30%), south-south-west (14.7%), and south-south-east (13.9%) in July, and south-south-west (14.3%), north (14.0%), and south (13.7%) in September. In order to verify the grid sizes used in previous studies (Table 1), the grid was divided into 12 scales from 25 m to 300 m with a step size of 25 m. The wind direction-weighted FAI was calculated under different grid sizes, as shown in Fig. 5.

According to Figs. 5, 6a, and b, when the grid size increases from 25 m to 300 m, the maximum FAI values in July are 13.850, 5.651, 2.878, 1.634, 1.091, 0.932, 0.871, 0.822, 0.480, 0.422, 0.531, and 0.335, respectively, and the maximum FAI values in September are 13.849, 5.789, 2.827, 1.723, 1.308, 0.981, 0.987, 0.847, 0.577, 0.518, 0.359, and 0.359, respectively. In areas with FAI $>$ 1, urban morphology has a strong hindrance to the wind, resulting in a poor ventilation environment. When the grid size increases from 25 m to 150 m, in July, the numbers of grids with FAI $>$ 1 are 19,992, 1538, 153, 20, 4, and 0, accounting for 2.106%, 0.645%, 0.081%, 0.019%, 0.006%, and 0% of the total, respectively. In September, the numbers of grids with FAI $>$ 1 are 17,633, 1643, 164, 22, 8, and 0, accounting for 1.849%, 0.689%, 0.155%, 0.037%, 0.021%, and 0% of the total, respectively. When the grid size is greater than or equal to 150 m, there is no grid with FAI $>$ 1. FAI is sensitive to changes in grid size. With increasing grid size, FAI tends to average out. With decreasing grid size, it tends to detect areas with excessive hindrance to the wind.

3.2. Land surface temperature distribution

We used a single-window algorithm to invert LST and normalized it using the extreme value method. The results are shown in Figs. 7 and 8.

According to Figs. 7 and 8, in July 2016, 98% of the pixels had a temperature between 295 K and 332 K, with an average temperature of 314 K. In September 2017, 98% of the pixels had a temperature between 297 K and 306 K, with an average temperature of 301 K. The average LST in Shahekou District and Xigang District was higher than the average. In July, the average temperatures in the two districts were 318.2 K and 318.4 K, respectively. In September, the average temperatures in the two districts were 303 K and 302 K, respectively. The spatial distribution of high temperature pixels is similar to that of buildings. The buildings in Shahekou District and Xigang District are dense; the low ventilation efficiency in the area leads to heat accumulation and temperature rise.

3.3. Correlation analysis and trend test

The normalized LST is resampled based on grid sizes. We calculated the nonlinear correlation coefficient between FAI and LST under different grid sizes. The results are shown in Fig. 9.

As shown in Fig. 9 and Table 4, when the grid size increases from 25 m to 300 m with a step size of 25 m, the 12 correlation coefficients are 0.305, 0.301, 0.287, 0.275, 0.242, 0.227, 0.208, 0.181, 0.193, 0.192, 0.191, and 0.190 in July, and 0.340, 0.318, 0.302, 0.286, 0.285, 0.288, 0.238, 0.288, 0.290, 0.268, 0.262, and 0.255 in September. When the grid size is 25 m, the correlation coefficients are the maximum, that is, 0.305 in July and 0.340 in September. Although the correlation coefficients are between 0.2 and 0.3, considering the complex and diverse factors affecting the urban LST, this single-element correlation analysis can be used to

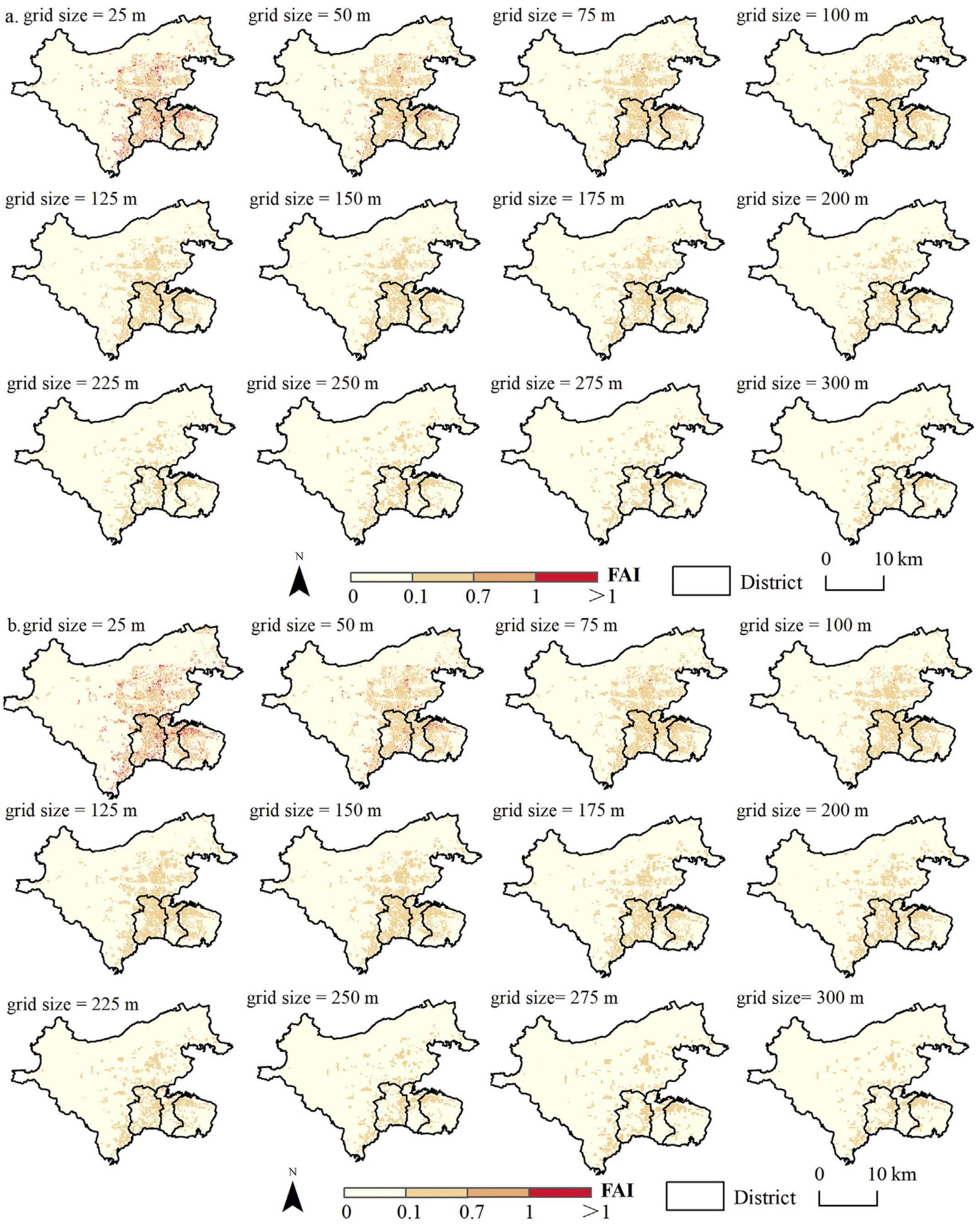

Fig. 5. FAI in different grid sizes (a. July, b. September).

explain the correlation between FAI and LST. The Mann–Kendall test was performed, and both sets of data passed the 99% significance test. The results show that as the grid size increases, the correlation between FAI and LST significantly decreases at the 0.01 significance level.

4. Discussions

4.1. Scale effect of FAI

There are various opinions on the scale selection for FAI calculation. Bottema and Mestayer (1998) adopted a grid size of 150 m. Wong et al. (2013, 2010) considered 100 m as the most effective grid size. Frey and Parlow (2010) believed that a grid size between

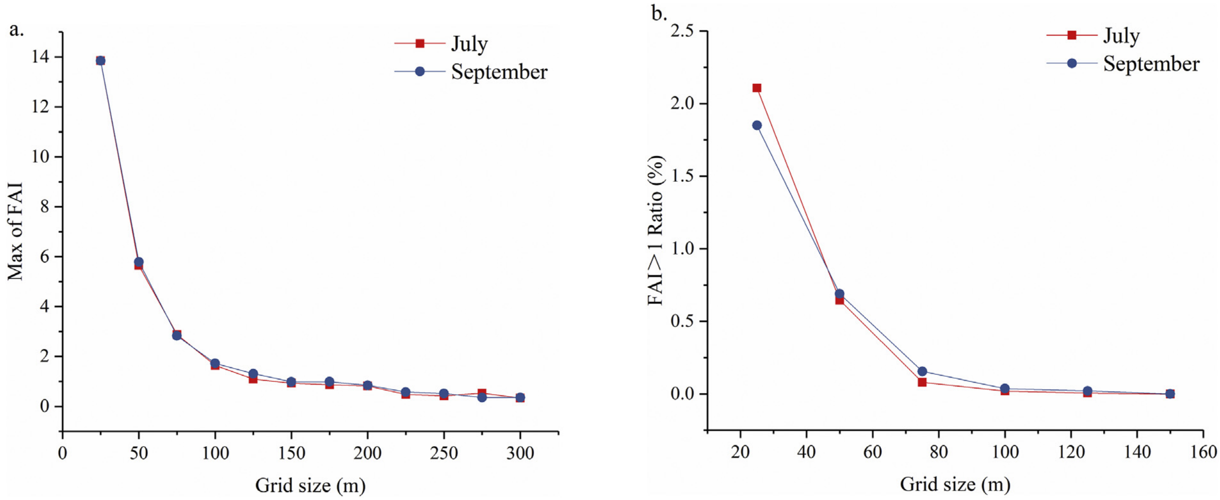

Fig. 6. Static of FAI in different grid sizes (*A. maximum* of FAI b. Area ratio of FAI > 1 cells).

75 and 125 m is the effective grid size for FAI calculation. Ng et al. (2011) considered 200 m to be an effective grid size through grid sensitivity test. Chen et al. (2017b) adopted a grid size of 50 m. Peng et al. (2017a) and Xu et al. (2017) used raster data for FAI calculation and obtained the same grid size with raw data resolution (30 m and 10 m). In this study, FAI calculations were performed under different grid sizes and it was found that there were differences in the threshold and distribution of FAI under different grid sizes. When the grid size is 25 m, the proportion of pixels with FAI > 1 is the largest. It shows that FAI is sensitive to changes in grid size. Under different grid sizes, the effectiveness of FAI is different; small-sized grids can better identify situations in which the local wind hindrance is large. A grid size of 25 m is likely to be more effective to determine areas with strong wind resistance, which is significantly different from the conclusions in other studies. The spatial distribution of buildings and the combination of buildings of different heights and form are potential influencing factors in these results.

4.2. Scale effect of correlation between FAI and LST

Most studies on LST have analyzed the correlation between LST and other factors at different resolutions, and have attempted to determine the correlation with grid size changes to find the best resolution, such as analyzing the correlations between LST and landscape pattern (Song et al., 2014; Wang et al., 2016) and LST and vegetation (Fan et al., 2015) at different resolutions. Urban morphology disturbs the local climate by disturbing ventilation. Good ventilation helps decrease heat and alleviates the high temperature caused by UHI. Previous studies have combined FAI with LST to analyze the correlation between the two using different grid sizes. Wong and Nichol (Wong et al., 2013) used the Kowloon Peninsula as an example to study the correlation between FAI and UHI. They found that the correlation between the two was the strongest when the grid size was 100 m. Owing to high building density and high-rise buildings, Kowloon Peninsula is significantly different from most cities in China. The architectural patterns and surface features of different cities are different, and therefore the scale effects show different results. In contrast, Dalian has a diverse building form and it is similar to those in most cities in China; therefore, the results of the scale effect study in Dalian has greater reference value for cities in China. Moreover, Dalian, as the study area is much larger than the study areas in previous studies, thereby providing much more samples to make the study results more reliable. Furthermore, since the relationship between FAI and LST is complex, a nonlinear correlation analysis was used instead of the linear correlation analysis to improve the study results.

4.3. Limitations

Due to limited availability of data, the data recorded from the meteorological site were used in this study to reflect the climatic background and there is room for further improvement regarding the accuracy of reflecting the wind environment inside the city. Wind speed has little influence on surface temperature and heat island (Yao et al., 2018) and the correlation analysis may have exhibited different results at different wind speed levels. The building data was derived from Baidu Maps, and since buildings, such as portable dwellings in urban and rural fringe areas, are not accurate, underestimating the buildings weakened the results of the correlation analysis. The building data only contains building outlines and floors and types, using floors and average floor height to calculate height of the buildings which may have a deviation with the actual height of the building and a uncertainty impact on FAI value. The Landsat-8/TIRS infrared remote sensing data with a resolution of 100 m is not accurate enough to reflect the infrared characteristics of buildings. Factors affecting the urban wind and heat environment are complex, such as topography, meteorology (He, 2018), vegetation (Yang et al., 2017; Yuan et al., 2017; Zhou et al., 2016), building materials (Erell et al., 2014), underlying surface properties, and man-made heat. Therefore, these factors should be considered in future studies. Moreover, the effect of grid size on the relationship between urban morphology and the heat environment needs to be further studied and analyzed using high-

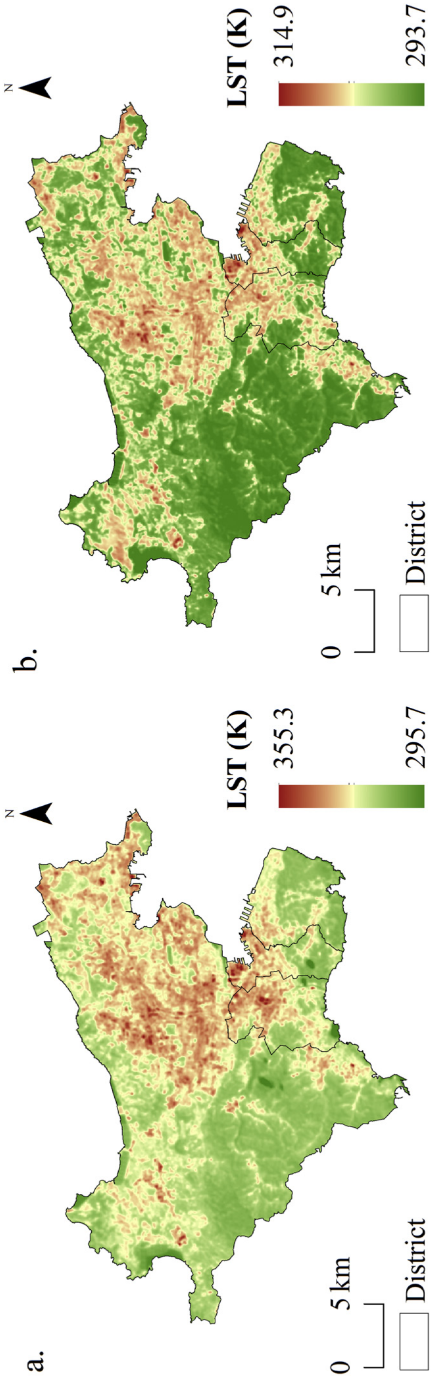

Fig. 7. Land surface temperature (a. 2016.7.2, b. 2017.9.23).

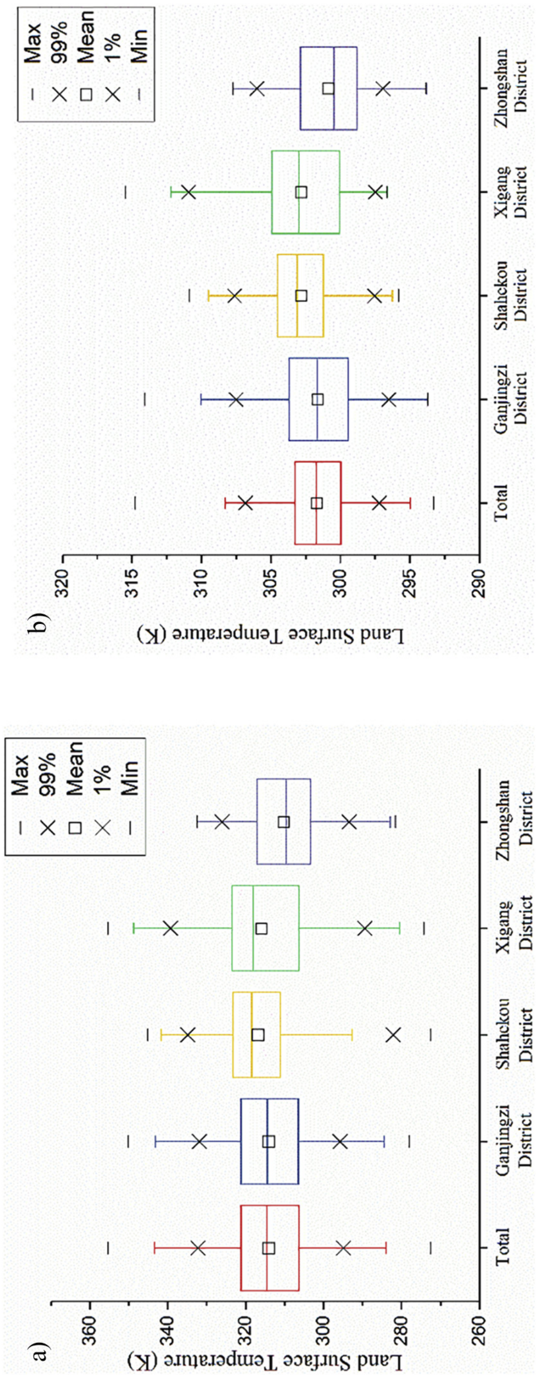

Fig. 8. Box plot of LST distribution (a. 2016.7.2, b. 2017.9.23).

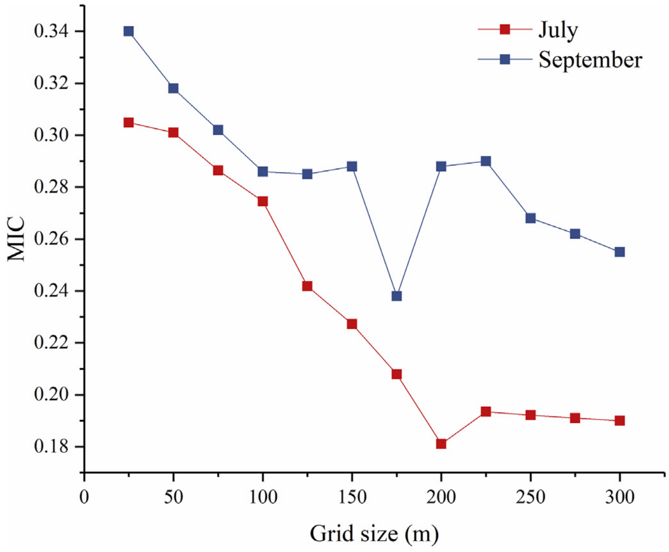

Fig. 9. Correlation between FAI and LST under different grid sizes.

Table 4
Results of the Mann–Kendall test.

Significant level in hypothesis test	Mann–Kendall generated *Z*-value		Accept/reject	
	2016.07.02	2017.09.23	2016.07.02	2017.09.23
1.645 (90%)	−2.674	−3.840	Accept	Accept
1.960 (95%)	−2.674	−3.840	Accept	Accept
2.576 (99%)	−2.674	−3.840	Accept	Accept

precision multivariate data sets.

5. Conclusions

Taking Dalian as an example, a nonlinear correlation analysis was used to study the correlation between FAI and LST under different grid sizes based on multi-source data, such as urban architecture and Landsat-8/TIRS thermal infrared remote sensing. The results of the study are as follows:

(1) FAI is sensitive to changes in grid size. Compared with larger grid sizes, a smaller size is more likely to detect changes in building form with strong wind hindrance. The grid size increases from 25 m to 300 m with a step size of 25 m, resulting in a total of 12 different sizes. There is a significant decreasing trend in the number and ratio of grids with FAI $>$ 1. When the grid size is greater than or equal to 150 m, there is no grid with FAI $>$ 1.

(2) FAI of the city is related to LST, and the correlations under different grid sizes are different. The correlation is strongest when the grid size is 25 m, indicating that a grid size of 25 $\times$ 25 m is the most effective grid size. The grid size increases from 25 m to 300 m with a step size of 25 m. The 12 correlation coefficients between LST and FAI were 0.305, 0.301, 0.287, 0.275, 0.242, 0.227, 0.208, 0.181, 0.193, 0.192, 0.191, and 0.190 in July, and 0.340, 0.318, 0.302, 0.286, 0.285, 0.288, 0.238, 0.288, 0.290, 0.268, 0.262, and 0.255 in September. When the grid size was 25 m, the correlation coefficients were the maximum, that is, 0.305 in July and 0.340 in September, respectively. The Mann–Kendall test showed that as the grid size increased, the correlation between FAI and LST decreased at the 0.01 significance level.

Conflicts of interest

The authors declare no competing financial interests.

This manuscript has not been published or presented elsewhere in part or in entirety and is not under consideration by another journal. The study design was approved by the appropriate ethics review board. We have read and understood your journal's policies, and we believe that neither the manuscript nor the study violates any of these. There are no conflicts of interest to declare.

Author contributions

Jun Yang contributed to all aspects of this work; Yichen Wang wrote the main manuscript text, conducted the experiment and analyzed the data; Xiangming Xiao, Cui Jin, Jianhong (Cecilia) Xia and Xueming Li revised the paper. All authors reviewed the manuscript.

Acknowledgments

This research study was supported by the National Natural Science Foundation of China (grant no. 41771178, 41630749, 41471140), Innovative Talents Support Program of Liaoning Province (Grant No. LR2017017) and the Liaoning Province Outstanding Youth Program (grant no. LJQ2015058). The authors would like to acknowledge all experts' contributions in the building of the model and the formulation of the strategies in this study.

References

Allegrini, J., Carmeliet, J., 2017. Coupled CFD and building energy simulations for studying the impacts of building height topology and buoyancy on local urban microclimates. Urban Clim. 21.
Bottema, M., Mestayer, P.G., 1998. Urban roughness mapping-validation techniques and some first results. J. Wind Eng. Ind. Aerodyn. 74–76, 163–173.
Brunet, Y., Finnigan, J.J., Raupach, M.R., 1994. A wind tunnel study of air flow in waving wheat: Singple-point velocity statistics. Boundary-Layer Meteorol. 70, 95–132.
Bureau of Urban Planning Dalian China, 2004. Dalian city planning and architectural design regulations.
Burian, S.J., Brown, M.J., Linger, S.P., 2002. Morphological analyses using 3D building databases. La-Ur-02-0781.
Cariolet, J.M., Colombert, M., Vuillet, M., Diab, Y., 2018. Assessing the resilience of urban areas to traffic-related air pollution: application in greater Paris. Sci. Total Environ. 615, 588–596. https://doi.org/10.1016/j.scitotenv.2017.09.334.
Chen, F., Liu, J., Ge, Q., 2017a. Pulling vs. pushing: effect of climate factors on periodical fluctuation of Russian and South Korean tourist demand in Hainan Island, China. Chinese Geogr. Sci. 27, 648–659. https://doi.org/10.1007/s11769-017-0892-8.
Chen, S.L., Lu, J., Yu, W.W., 2017b. A quantitative method to detect the ventilation paths in a mountainous urban city for urban planning: a case study in Guizhou, China. Indoor Built Environ. 26, 422–437. https://doi.org/10.1177/1420326X15626233.
Chen, Y.C., Lin, T.P., Lin, C.T., 2017c. A simple approach for the development of urban climatic maps based on the urban characteristics in Tainan, Taiwan. Int. J. Biometeorol. 61, 1029–1041. https://doi.org/10.1007/s00484-016-1282-0.
Clarke, J.F., Bach, W., 1971. Comparison of the comfort conditions in different urban and suburban microenvironments. Int. J. Biometeorol. 15, 41–54. https://doi.org/10.1007/BF01804717.
Dhunny, A.Z., Samkhaniani, N., Lollchund, M.R., Rughooputh, S.D.D.V., 2018. Investigation of multi-level wind flow characteristics and pedestrian comfort in a tropical city. Urban Clim. 24, 185–204. https://doi.org/10.1016/j.uclim.2018.03.002.
Erell, E., Pearlmutter, D., Boneh, D., Kutiel, P.B., 2014. Effect of high-albedo materials on pedestrian heat stress in urban street canyons. Urban Clim. 10, 367–386.
Estoque, R.C., Murayama, Y., Myint, S.W., 2017. Effects of landscape composition and pattern on land surface temperature : an urban heat island study in the megacities of Southeast Asia. Sci. Total Environ. 577, 349–359. https://doi.org/10.1016/j.scitotenv.2016.10.195.
Fan, C., Myint, S.W., Zheng, B., 2015. Measuring the spatial arrangement of urban vegetation and its impacts on seasonal surface temperatures. Prog. Phys. Geogr. 39, 199–219. https://doi.org/10.1177/0309133314567583.
Frey, C., Parlow, E., 2010. Determination of the aerodynamic resistance to heat using morphometric methods. EARSeL eProceedings 52–63.
Gál, T., Unger, J., 2009. Detection of ventilation paths using high-resolution roughness parameter mapping in a large urban area. Build. Environ. 44, 198–206. https://doi.org/10.1016/j.buildenv.2008.02.008.
Grimmond, C.S.B., Oke, T.R., 1999. Aerodynamic properties of urban areas derived from analysis of surface form. J. Appl. Meteorol. 38, 1262–1292. https://doi.org/10.1175/1520-0450(1999)038<1262:APOUAD>2.0.CO;2.
Gromke, C., 2018. Wind tunnel model of the forest and its Reynolds number sensitivity. J. Wind Eng. Ind. Aerodyn. 175, 53–64. https://doi.org/10.1016/j.jweia.2018.01.036.
He, B.J., 2018. Potentials of meteorological characteristics and synoptic conditions to mitigate urban heat island effects. Urban Clim. 24, 26–33.
He, B.J., Ding, L., Prasad, D., 2019. Enhancing urban ventilation performance through the development of precinct ventilation zones: A case study based on the Greater Sydney, Australia. Sustain. Cities Soc. 47, 101472. https://doi.org/10.1016/j.scs.2019.101472.
Hsieh, C.M., Huang, H.C., 2016. Mitigating urban heat islands: a method to identify potential wind corridor for cooling and ventilation. Comput. Environ. Urban. Syst. 57, 130–143. https://doi.org/10.1016/j.compenvurbsys.2016.02.005.
Hu, D., Qiao, K., Wang, X., Zhao, L., Ji, G., 2015. Land surface temperature retrieval from Landsat 8 thermal infrared data using mono-window algorithm. J. Remote Sens. 19, 964–976. https://doi.org/10.11834/jrs.20155038.
Ikegaya, N., Ikeda, Y., Hagishima, A., Razak, A.A., Tanimoto, J., 2017. A prediction model for wind speed ratios at pedestrian level with simplified urban canopies. Theor. Appl. Climatol. 127, 655–665. https://doi.org/10.1007/s00704-015-1655-z.
Jandaghian, Z., Akbari, H., 2018. The effects of increasing surface reflectivity on heat-related mortality in greater Montreal area, Canada. Urban Clim. 25, 135–151.
Kendall, M.G., 1975. Rank Correlation Measures. Charles Griffin, London, pp. 202 202.
Konopacki, S., Akbari, H., 2000. Energy savings calculations for heat island reduction strategies in Baton Rouge. In: Sacramento and Salt Lake City. Proc. ACEEE Summer Study Energy Effic Build. vol. 9. pp. 9.215–9.226. https://doi.org/10.1017/CBO9781107415324.004.
Lan, Y., Zhan, Q., 2017. How do urban buildings impact summer air temperature? The effects of building configurations in space and time. Build. Environ. 125, 88–98. https://doi.org/10.1016/j.buildenv.2017.08.046.
Lettau, 1969. Note on aerodynamic roughness-parameter estimation on the basis of roughness-element description. J. Appl. Meteorol. 8, 828–832 (doi:http://dx.doi.org/10.1175/1520-0450(1969)008 < 0828:NOARPE > 2.0.CO;2).
Li, H., Meier, F., Lee, X., Chakraborty, T., Liu, J., Schaap, M., Sodoudi, S., 2018a. Interaction between urban heat island and urban pollution island during summer in Berlin. Sci. Total Environ. 636, 818–828. https://doi.org/10.1016/j.scitotenv.2018.04.254.
Li, H., Zhou, Y., Li, X., Meng, L., Wang, X., Wu, S., Sodoudi, S., 2018b. A new method to quantify surface urban heat island intensity. Sci. Total Environ. 624, 262–272. https://doi.org/10.1016/j.scitotenv.2017.11.360.
Li, H., Zhou, Y., Wang, X., Zhou, X., Zhang, H., Sodoudi, S., 2019. Quantifying urban heat island intensity and its physical mechanism using WRF/UCM. Sci. Total Environ. 650, 3110–3119. https://doi.org/10.1016/j.scitotenv.2018.10.025.
Liu, J., Wang, J., Wang, S., Wang, J., Deng, G., 2018. Analysis and simulation of the spatiotemporal evolution pattern of tourism lands at the Natural World Heritage Site Jiuzhaigou, China. Habitat Int 79, 74–88. https://doi.org/10.1016/j.habitatint.2018.07.005.
Macdonald, R.W., Griffiths, R.F., Hall, D.J., 1998. An improved method for the estimation of surface roughness of obstacle arrays. Atmos. Environ. 32, 1857–1864. https://doi.org/10.1016/S1352-2310(97)00403-2.
Ng, E., Chen, L., Ren, C., Fung, J.C.H., Yuan, C., 2011. Improving the Wind Environment in High-Density Cities by Understanding Urban Morphology and Surface Roughness: A Study in Hong Kong. Landsc. Urban Planning. vol. 101. Elsevier Sci. Ltd, pp. 59–74.

Peng, F., Wong, M.S., Wan, Y., Nichol, J.E., 2017a. Modeling of urban wind ventilation using high resolution airborne LiDAR data. Comput. Environ. Urban. Syst. 64, 81–90. https://doi.org/10.1016/j.compenvurbsys.2017.01.003.

Peng, F., Wong, M.S., Wan, Y., Nichol, J.E., Sing, M., Wan, Y., Nichol, J.E., Wong, M.S., Wan, Y., Nichol, J.E., Sing, M., Wan, Y., Nichol, J.E., 2017b. Modeling of urban wind ventilation using high resolution airborne LiDAR data. Comput. Environ. Urban. Syst. 64, 81–90. https://doi.org/10.1016/j.compenvurbsys.2017.01.003.

Qiao, Z., Tian, G., Xiao, L., 2013. Diurnal and seasonal impacts of urbanization on the urban thermal environment: a case study of Beijing using MODIS data. ISPRS J. Photogramm. Remote Sens. 85, 93–101. https://doi.org/10.1016/j.isprsjprs.2013.08.010.

Qiao, Z., Xu, X., Wu, F., Luo, W., Wang, F., Liu, L., Sun, Z., 2017. Urban ventilation network model: a case study of the core zone of capital function in Beijing metropolitan area. J. Clean. Prod. 168, 526–535. https://doi.org/10.1016/j.jclepro.2017.09.006.

Qin, Z., Karnieli, A., Berliner, P., 2001. A mono-window algorithm for retrieving land surface temeprature from Landsat TM and its application to the Israel-Egypt border region. Int. J. Remote Sens. 18, 3719–3746.

Ratti, C., Di Sabatino, S., Britter, R., Brown, M., Burian, S., Caton, F., 2002. Analysis of 3-D urban databases with respect to pollution dispersion for a number of European and American cities. Water, Air, Soil Pollut. Focus 2, 459–469. https://doi.org/10.1023/A:1021380611553.

Reshef, D.N., Reshef, Y.A., Finucane, H.K., Grossman, S.R., Mcvean, G., Turnbaugh, P.J., Lander, E.S., Mitzenmacher, M., 2011. Detecting novel associations in large data sets detecting novel associations in large data sets. Science (80-) 334, 1518–1524. https://doi.org/10.1126/science.1205438.

Rizwan, A.M., Dennis, L.Y.C., Liu, C., Memon, R.A., Leung, D.Y., Chunho, L., 2008. A review on the generation, determination and mitigation of urban Heat Island. J. Environ. Sci. 20, 120–128. https://doi.org/10.1016/S1001-0742(08)60019-4.

Song, J., Du, S., Feng, X., Guo, L., 2014. The relationships between landscape compositions and land surface temperature: quantifying their resolution sensitivity with spatial regression models. Landsc. Urban Plan. 123, 145–157. https://doi.org/10.1016/j.landurbplan.2013.11.014.

Tan, J., Zheng, Y., Tang, X., Guo, C., Li, L., Song, G., Zhen, X., Yuan, D., Kalkstein, A.J., Li, F., Chen, H., 2010. The urban heat island and its impact on heat waves and human health in Shanghai. Int. J. Biometeorol. https://doi.org/10.1007/s00484-009-0256-x.

Voogt, J.A., Oke, T.R., 2003. Thermal remote sensing of urban climates. Remote Sens. Environ. 86, 370–384. https://doi.org/10.1016/S0034-4257(03)00079-8.

Wang, F., Qin, Z., Song, C., Tu, L., Karnieli, A., Zhao, S., 2015. An improved mono-window algorithm for land surface temperature retrieval from Landsat 8 thermal infrared sensor data. Remote Sens. 7, 4268–4289. https://doi.org/10.3390/rs70404268.

Wang, J., Qingming, Z., Guo, H., Jin, Z., 2016. Characterizing the spatial dynamics of land surface temperature–impervious surface fraction relationship. Int. J. Appl. Earth Obs. Geoinf. 45, 55–65. https://doi.org/10.1016/j.jag.2015.11.006.

Wang, W., Xu, Y., Ng, E., Raasch, S., 2018. Evaluation of satellite-derived building height extraction by CFD simulations: a case study of neighborhood-scale ventilation in Hong Kong. Landsc. Urban Plan. 170, 90–102. https://doi.org/10.1016/j.landurbplan.2017.11.008.

Wong, M.S., Nichol, J.E., To, P.H, Wang, J., 2010. A simple method for designation of urban ventilation corridors and its application to urban heat island analysis. Build. Environ. 45, 1880–1889. https://doi.org/10.1016/j.buildenv.2010.02.019.

Wong, M.S., Nichol, J.E., SingWong, M., Nichol, J.E., 2013. Spatial variability of frontal area index and its relationship with urban heat island intensity. Int. J. Remote Sens. 34, 885–896. https://doi.org/10.1080/01431161.2012.714509.

Wu, J., 2004. Effects of changing scale on landscape pattern analysis: scaling relations. Landsc. Ecol. 19, 125–138. https://doi.org/10.1023/B:LAND.0000021711.40074.ae.

Xu, Y., Ren, C., Ma, P., Ho, J., Wang, W., Lau, K.K., Lin, H., Ng, E., 2017. Urban morphology detection and computation for urban climate research. Landsc. Urban Plan. 167, 212–224. https://doi.org/10.1016/j.landurbplan.2017.06.018.

Yao, R., Wang, L., Huang, X., Niu, Y., Chen, Y., Niu, Z., 2018. The influence of different data and method on estimating the surface urban heat island intensity. Ecol. Indic. 89, 45–55. https://doi.org/10.1016/j.ecolind.2018.01.044.

Yang, J., Sun, J., Ge, Q., Li, X., 2017. Assessing the impacts of urbanization-associated green space on urban land surface temperature: A case study of Dalian, China. Urban For. Urban Green. 22, 1–10. https://doi.org/10.1016/j.ufug.2017.01.002.

Yang, J., Guo, A., Li, Y., Zhang, Y., Li, X., 2018a. Simulation of landscape spatial layout evolution in rural-urban fringe areas: a case study of Ganjingzi District. GIScience Remote Sens 11, 1–18. https://doi.org/10.1080/15481603.2018.1533680.

Yang, J., Su, J., Xia, J.C., Jin, C., Li, X., Ge, Q., 2018b. The Impact of Spatial Form of Urban Architecture on the Urban Thermal Environment : A Case Study of the Zhongshan District, Dalian, China. IEEE J. Sel. Top. Appl. Earth Obs. Remote Sens 99, 1–8.

Yang, J., Jin, S., Xiao, X., Jin, C., (Cecilia) Xia, J., Li, X., Wang, S., 2019. Local Climate Zone Ventilation and Urban Land Surface Temperatures: Towards a Performance-based and Wind-sensitive Planning Proposal in Megacities. Sustain. Cities Soc. 47, 1–11. https://doi.org/10.1016/j.scs.2019.101487.

Yuan, C., Ren, C., Ng, E., 2014. GIS-based surface roughness evaluation in the urban planning system to improve the wind environment – a study in Wuhan, China. Urban Clim. 10, 585–593.

Yuan, C., Norford, L., Ng, E., 2017. A semi-empirical model for the effect of trees on the urban wind environment. Landsc. Urban Plan. 168, 84–93. https://doi.org/10.1016/j.landurbplan.2017.09.029.

Zhang, G., Hao, Z., Zhu, S., 2016. Influence of urban spatial morphology on air temperature variance. Curr. Sci. 110, 619–626. https://doi.org/10.18520/cs/v110/i4/619-626.

Zhou, D., Zhao, S., Liu, S., Zhang, L., Zhu, C., 2014. Surface urban heat island in China's 32 major cities: spatial patterns and drivers. Remote Sens. Environ. 152, 51–61. https://doi.org/10.1016/j.rse.2014.05.017.

Zhou, D., Zhang, L., Li, D., Huang, D., Zhu, C., 2016. Climate-vegetation control on the diurnal and seasonal variations of surface urban heat islands in China. Environ. Res. Lett. 11. https://doi.org/10.1088/1748-9326/11/7/074009.